frontiers | Frontiers in Physics

TYPE Original Research
PUBLISHED 27 July 2023
DOI 10.3389/fphy.2023.1227140

OPEN ACCESS

EDITED BY
Bing Guo,
China Institute of Atomic Energy, China

REVIEWED BY
Wenjun Ma,
Peking University, China
Mrutunjaya Bhuyan,
University of Malaya, Malaysia

*CORRESPONDENCE
Marco Tosca,
Marco.Tosca@eli-beams.eu
Andrei Choukourov,
choukourov@kmf.troja.mff.cuni.cz

†PRESENT ADDRESS
Anna Macková,
Department of Physics, Faculty of Science,
J. E. Purkyně University,
Ústí nad Labem, Czechia

RECEIVED 22 May 2023
ACCEPTED 12 July 2023
PUBLISHED 27 July 2023

CITATION
Tosca M, Molloy D, McNamee A, Pleskunov P, Protsak M, Biliak K, Nikitin D, Kousal J, Krtouš Z, Hanyková L, Hanuš J, Biederman H, Foster T, Nersisyan G, Martin P, Ho C, Macková A, Mikšová R, Borghesi M, Kar S, Istokskaia V, Levy Y, Picciotto A, Giuffrida L, Margarone D and Choukourov A (2023), Plasma polymers as targets for laser-driven proton-boron fusion.
Front. Phys. 11:1227140.
doi: 10.3389/fphy.2023.1227140

Plasma polymers as targets for laser-driven proton-boron fusion

Marco Tosca[1,2,3]*, Daniel Molloy[4,5], Aaron McNamee[4], Pavel Pleskunov[1], Mariia Protsak[1], Kateryna Biliak[1], Daniil Nikitin[1], Jaroslav Kousal[1], Zdeněk Krtouš[1], Lenka Hanyková[1], Jan Hanuš[1], Hynek Biederman[1], Temour Foster[4], Gagik Nersisyan[4], Philip Martin[4], Chloe Ho[4], Anna Macková[6†], Romana Mikšová[6], Marco Borghesi[4], Satyabrata Kar[4], Valeriia Istokskaia[2,6], Yoann Levy[7], Antonino Picciotto[9], Lorenzo Giuffrida[2,10], Daniele Margarone[2,4,10] and Andrei Choukourov[1]*

[1]Department of Macromolecular Physics, Faculty of Mathematics and Physics, Charles University, Prague, Czechia, [2]ELI Beamlines Facility, The Extreme Light Infrastructure ERIC, Dolni Brezany, Czechia, [3]Marvel Fusion GmbH, Munich, Germany, [4]Centre for Light Matter Interaction, School of Mathematics and Physics, Queen's University Belfast, Belfast, United Kingdom, [5]HB11 Energy Holdings Pty, Freshwater, NSW, Australia, [6]Department of Neutron Physics, Nuclear Physics Institute (NPI) of the Czech Academy of Sciences, Husinec-Rez, Czechia, [7]Czech Technical University in Prague, Faculty of Nuclear Sciences and Physical Engineering, Prague, Czechia, [8]HiLASE Centre, Institute of Physics (FZU), Czech Academy of Sciences, Dolni Brezany, Czechia, [9]Micro-Nano Facility—Sensors and Devices Center, Fondazione Bruno Kessler (FBK), Trento, Italy, [10]Istituto Nazionale di Fisica Nucleare- Laboratori Nazionali dei Sud, Catania, Italy

Laser-driven proton-boron (pB) fusion has been gaining significant interest for energetic alpha particles production because of its neutron-less nature. This approach requires the use of B- and H-rich materials as targets, and common practice is the use of BN and conventional polymers. In this work, we chose plasma-assisted vapour phase deposition to prepare films of oligoethylenes (plasma polymers) on Boron Nitride BN substrates as an advanced alternative. The r.f. power delivered to the plasma was varied between 0 and 50 W to produce coatings with different crosslink density and hydrogen content, while maintaining the constant thickness of 1 µm. The chemical composition, including the hydrogen concentration, was investigated using XPS and RBS/ERDA, whereas the surface topography was analyzed using SEM and AFM. We triggered the pB nuclear fusion reaction focusing laser pulses from two different systems (i.e., the TARANIS multi-TW laser at the Queen's University Belfast (United Kingdom) and the PERLA B 10-GW laser system at the HiLASE center in Prague (Czech Republic)) directly onto these targets. We achieved a yield up to 10^8 and 10^4 alpha particles/sr using the TARANIS and PERLA B lasers, respectively. Radiative-hydrodynamic and particle-in-cell PIC simulations were performed to understand the laser-target interaction and retrieve the energy spectra of the protons. The nuclear collisional algorithm implemented in the WarpX PIC code was used to identify the region where pB fusion occurs. Taken together, the results suggest a complex relationship between the hydrogen content, target morphology, and structure of the plasma polymer, which play a crucial role in laser absorption, target expansion, proton acceleration and ultimately nuclear fusion reactions in the plasma.

KEYWORDS

plasma polymer, thin films, boron nitride, proton-boron fusion, ultra-high intense lasers

1 Introduction

At present, the world is facing a global energy crisis due to our dependence on non-renewable energy sources. One of the possible solutions may be found in the exploitation of nuclear fusion energy sources using magnetic confinement [1] or inertial confinement [2] approaches using deuterium-tritium (DT) as fuel. Proton-boron (pB) nuclear fusion requires a higher plasma temperature to achieve ignition compared to DT fusion, however, remains an exciting approach based on the generation of alpha particles, with a low neutron yield (<0.1%), thus without radioactive activation or waste. Additionally, the fuel isotopes are abundantly available (H and B) [3]. The three main schemes of the reaction are:

$$p+^{11}B \rightarrow 3\alpha + 8.7\,MeV$$
$$p+^{11}B \rightarrow \alpha_0 + {}^{8}Be + 8.6\,MeV \rightarrow \alpha_0 + \alpha_{01} + \alpha_{02}$$
$$p+^{11}B \rightarrow \alpha_1 + {}^{8}Be^{*} + 5.7\,MeV \rightarrow \alpha_1 + \alpha_{11} + \alpha_{12}$$

The overall products are three energetic alpha particles. The alpha particles can be captured by a magnetic field and used as a source of renewable energy [4] or in general be used to build an "ultraclean" fusion reactor [5–8]. Otherwise, fusion generated alpha particles are extremely useful in numerous biomedical applications, including radiobiology and cancer treatment [9–11], or could also be used for neutron-less nuclear-fusion-based propulsion in space [12]. Additionally, the generation of an energetic alpha particles source could pave the route towards societal applications, such as non-destructive material analysis [13] and radioisotopes production for imaging or therapy [14, 15]. However, such a thermal nuclear fusion approach is difficult because of the enormous temperatures required to trigger pB fusion when compared to DT-based approaches.

Non-thermal laser-driven pB fusion has been gaining significant interest in recent years. The basis of the process is the irradiation of materials rich in boron and hydrogen with high-energy pulsed lasers. The mechanisms of laser-driven ion acceleration depend on the target thickness and laser characteristic (pulse duration and energy delivered on target). For macroscopic thick targets (>100 μm), the generated ions can be accelerated in the backward direction due to a combination of the Coulomb explosion mechanisms and space-charge effects (hot electrons escaping the plasma) [16, 17]. Since the first laser-driven pB fusion experiment in 2005 [18], many other experiments have been carried out with improved diagnostics, experimental setup, targets, and laser systems [19–24] reaching a maximum alpha particles yield of 3×10^{10} α/sr/shot [25].

In previous pB fusion experiments commercially available Boron Nitride (BN) has been used in the in-target geometry [25]. The properties and benefits of BN as a boron-rich material are well known [26]. In such targets the hydrogen concentration depends on contamination during the material synthesis. Recent improvements in DT fusion show the importance of target manufacturing in optimizing the fusion yield [27]. Considering pB fusion, an area for optimization is through controlling the hydrogen-boron ratio to increase the alpha particles yield for a given laser. One option is through the use of polymers which have a large diversity of chemical composition and a wide range of inherent time and length scales make them extremely interesting as tunable reservoirs of hydrogen [28]. For example, poly(ethylene) is an aliphatic polymer with a very high (67 at%) hydrogen content. The first pB experiments used commercially available polymers in the form of macroscopic foils or sheets and combined them with BN in a composite target (in-target configuration) [18] or as a tandem unit (pitcher-catcher configuration) [29]. Recently, plasma-assisted vapor phase deposition [28], [30–32] has been used to prepare thin films of hydrocarbon plasma polymers (ppC:H) on BN substrates and successfully used this in-target geometry to trigger pB fusion with a compact tabletop laser [33]. The method benefits from precise control of the thickness and chemical composition of the deposited plasma polymers, providing an environmentally benign workflow. Furthermore, low-temperature plasma-based methods offer non-equilibrium media to mix thermodynamically immiscible materials [34, 35], boron and hydrocarbons being an example, which might be indispensable in the future preparation of highly customized micro- and nanostructured targets.

The research presented here is the first attempt to obtain a deeper understanding of the role of the chemical composition, structure, and density of ppC:H thin films in the mechanism of the pB reaction and how the alpha particles yield can be affected when triggered by two laser of significantly different peak powers values (i.e., multi-TW TARANIS [36] and 10-GW PERLA B [37] laser systems) and pulse (or prepulse) temporal shape.

2 Materials and methods

2.1 Sample preparation

Thin films of hydrocarbon plasma polymers were deposited on BN substrates (1.5 mm thick, Fondazione Bruno Kessler FBK) using plasma-assisted vapor phase deposition of poly(ethylene) (PE, Sigma-Aldrich, $M_n = 2 \times 10^4$ g/mol). The generic scheme of the process is shown in Figure 1A. Before deposition, granules of PE were loaded into a crucible which was positioned above a graphite electrode. The deposition chamber was pumped to a base pressure of 10^{-4} Pa using a tandem of rotary and diffusion pumps, and then Ar was introduced at a flow rate of 10 sccm, setting the working pressure at 5.2 Pa. The crucible was heated to achieve a release of oligoethylenes, which was monitored by Quartz Crystal Microbalance (QCM). After a pre-heating stage, the temperature of the crucible was set at 300°C to maintain the constant deposition rate of oligoethylenes of 16 nm/min. In the case of experiments with plasma, an r.f. discharge (13.56 MHz) was initiated by delivering power from an r.f. power supply (R600 Kurt J. Lesker) to the graphite covered electrode through an automatic matching unit (R600 m KJL). Then substrates were introduced into the chamber using a loadlock and the depositions were performed.

2.2 Sample characterization

The thickness of thin films was measured by spectroscopic ellipsometry (Woolam M-2000DI) on samples deposited on polished silicon substrates to avoid difficulties related with the surface roughness. The measurements were done at three angles ranging from 50° to 70° and in the wavelength range of 192–1690 nm. The ellipsometry data were fitted using Complete

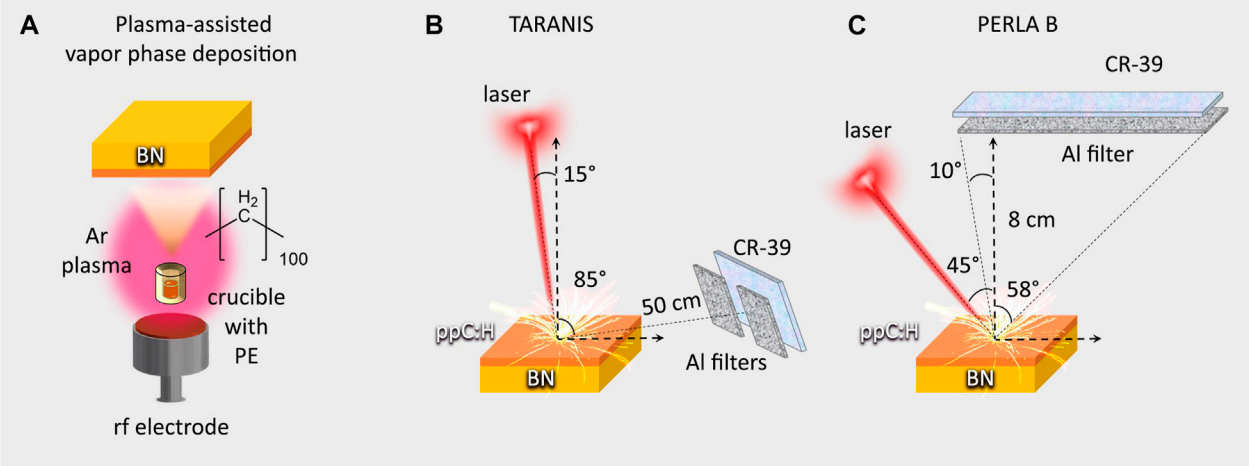

FIGURE 1
Design of the experiments: **(A)** plasma-assisted vapor phase deposition of ppC:H films on BN; **(B)** scheme of the TARANIS laser experiment; **(C)** scheme of the PERLA B laser experiment.

EASE software (J.A. Woollam) according to a Cauchy model for silicon substrate with 1.5 nm of native oxide. For the calculations of the film density, the samples of known thickness were deposited on Al foils with known surface area. The density of the films was measured gravimetrically by taking the Al foil weight difference before and after deposition (micro-scale Sartorius, CP225D-0CE, 0.01 mg) and dividing it by the film volume.

The surface topography of ppC:H thin films on BN was measured using Atomic Force Microscopy AFM and Scanning Electric Microscope equipped with Energy Dispersive X-ray detector SEM-EDX. The AFM measurements were performed in an intermittent contact mode (Ntegra, NT-MDT) using standard silicon cantilevers (Multi75-Al-G, BudgetSensors) in air. Images of 256 × 256 data points were acquired with different scan sizes. Second-order polynomials were subtracted from the raw data to remove the sample tilt. The SEM/EDX measurements (JSM-7200F SEM with JED-2300 EDX, Jeol) were carried out in a side-view orientation with a 10 kV acceleration voltage after the sample metallization with a 10 nm gold layer.

The chemical composition of ppC:H thin films was studied by Fourier-Transform Infrared spectroscopy (FTIR), X-ray photoelectron spectroscopy (XPS), Rutherford Back-scattering spectrometry (RBS) and Elastic recoil detection analysis (ERDA). The FTIR measurements (Bruker Equinox 55) were performed in a reflectance–absorbance mode on samples deposited on gold-mirror-covered silicon with a resolution of 4 cm^{-1} and with 200 scans. The XPS spectra (XPS, Phoibos 150, Specs) were acquired using an Al Kα X-ray source (1486.6 eV, Specs). Wide and high-resolution spectra were acquired with a pass energy of 40 eV and 10 eV, respectively. The spectra were analyzed using CasaXPS software and charge-referenced to aliphatic carbon at 285.0 eV. RBS/ERDA was performed using a tandem accelerator, Tandetron MC 4130. For RBS, He^+ ions were used at an energy of 3.07 MeV for the identification of O, whereas H^+ ions were used at an energy of 1.74 MeV for the detection of C using non-Rutherford cross section for elastic scattering advantageously offering enhancement of light element sensitivity detection. The scattered beam ions were detected by an ORTEC ULTRA-series detector with an active area of 50 mm^2 and a thickness of the depletion layer of 300 μm. The detector was placed at a backscattering angle of 170° out of a plane (the Cornell geometry). In the ERDA method, He^+ ions were used at an energy of 2.5 MeV for the depth profiling of H up to the analytical depth at about 500 nm. The detector was placed at a backscattering angle of 30° in a plane (the IBM geometry). All samples were measured at three different spots to avoid any damage during measurements and the final spectrum was provided as a sum of articular spectra from different beam spots. The RBS/ERDA recorded spectrum analysis was done using a SIMNRA code [38].

2.3 Laser-driven pB fusion reaction

Calibrated CR-39 (polyallyl diglycol carbonate) is a solid-state nuclear track detector able to detect and distinguish alpha particles emitted from laser-driven pB fusion with respect to other particles from the plasma emission [39]. Energetic nuclei disrupt chemical bonds when passing through the polymer, leaving tracks of broken polymer structure. These tracks can be exposed by removing the damaged material in alkali solutions. Irradiation of CR-39 with known sources of energetic nuclei allows for a spectroscopic calibration, which can be subsequently used to discriminate the traces from alpha particles obtained in pB experiments.

Experiments here described were performed focusing the laser beam tightly to the target surface. In such a scheme, the pB reaction occurs in the plasma environment and consequently, the generated alpha particles are affected by the plasma conditions. This scheme is called “in-target” configuration. The mm-thick target allows the detection of ions only in the front side of the target (for instance the same hemisphere of the laser direction). Two different experimental setups were used as depicted in Figures 1B, C, respectively for the TARANIS laser at Queen’s University Belfast (United Kingdom) and for the PERLA B laser at HiLASE, Dolni Brezany (Czech

TABLE 1 Cutoff energies of Al filters for different ion species calculated by LISE++.

Ions	Cutoff energy (MeV)	
	6.5 μm Al	14 μm Al
Proton	0.6	1.0
Alpha particles	1.8	3.7
Carbon	7.5	16.3
Nitrogen	9.0	20.0

Republic). The TARANIS laser pulse has a wavelength of 1.053 μm, temporal width of 800 fs, energy of 8 J/pulse and can reach intensities around $2 \times 10^{19}\, W/cm^2$ on target. The laser pulse was focused onto the ppC:H/BN target at an incidence angle of 15° with respect to the target normal. The CR-39 detector was placed at angle of 85° with respect to the target normal and a distance of 50 cm. A large detection angle relative to the target normal was used to reduce the flux of other backwards accelerated ions (e.g., carbon, boron, nitrogen, etc.) on the CR-39 detector. Three consecutive shots were fired in the same target conditions to improve the statistics of traces on the CR-39 detector with a repetition rate of 1 shot per 20 min. The BN target used at the TARANIS laser system had a 1 μm ppC:H layer deposition on the front surface. The PERLA B laser pulse has a wavelength of 1.030 μm, temporal width of 1.6 ps, energy of 17 mJ/pulse and can reach intensities around $2 \times 10^{16}\, W/cm^2$ on target. The incident angle was set to 45° with respect to the ppC:H/BN target normal and several hundreds of shots were made per each target at a repetition rate of 1 Hz. In this case the ppC:H layer was 680 nm in thickness. The CR-39 detector was positioned on the front of the target in the laser backward direction, covering large angle from −10°–58° as shown in Figure 1C. In both cases, diamond detectors working in a Time of Flight (TOF) geometry were installed to check the interaction shot-to-shot. Al foils of different thicknesses were placed as filters in front of the CR-39 detector sensitive surface to study the alpha particles energy distribution based on the cutoff energy determined by the Al foil thickness, and also to avoid saturation of the detector by undesired low energy plasma particles. The cutoff energy of the Al filters was calculated using LISE++ [40] and the results are shown in Table 1.

The CR-39 detectors were etched in 6.25 M NaOH at 70°C for 1 h (TARANIS) and 3 h (PERLA B). The calibration for alpha particles and protons was performed in the range of energies from 0.3 to 5.0 MeV, according to the described in [41]. Detailed analysis of the calculation of the total alpha particles yield can be found in [29].

2.4 Numerical simulations

The laser plasma interaction can be modeled using a combination of 2D radiative-hydrodynamic and particle-in-cell (PIC) simulations. The PERLA B laser system has a 1.5 picosecond prepulse arriving 14 ns before the main pulse with a contrast of ~10^{-3}. The prepulse interaction and subsequent plasma expansion was modelled using a 2D radiative-hydrodynamic simulation carried out with the FLASH code [42]. A particle-in-cell simulation based on the SMILEI PIC code was used to model the interaction with the main laser pulse thanks to the output of the FLASH simulation. A detailed description of the simulations and full results are presented in [33].

Similarly, the interaction between the TARANIS laser and the ppC:H/BN targets was modelled using a combination of the FLASH 2D radiative-hydrodynamic and WarpX ([43] PIC simulations codes respectively).

The TARANIS laser system has a ns pedestal with a contrast of ~10^{-7}. Therefore, the effect of the pedestal on the thin ppC:H deposition layer needs to be considered. The interaction between a 1.5 ns pedestal with a ppC:H layer at 15° incidence to the target normal was modelled using the FLASH code in 2D Cartesian geometry for three ppC:H densities of 600, 900 and 1,650 kg/m^3. An initial ionization fraction of ~4% was used to ensure that the target was not transparent to incident radiation in FLASH. The FLASH code uses adaptive mesh refinement to increase resolution in regions with large temperature or density gradients. In these simulations the minimum grid cell size was 100 nm × 100 nm.

The output of the FLASH simulation was used to set the initial conditions of the PIC simulation. Using the WarpX [43] PIC code, the interaction between the target and the main laser pulse (8 J, 800 fs FWHM, 6.5 μm FWHM), and incident on the target at 15° to target normal, was modeled. A simulation box of approximately 50 μm × 80 μm and cell size of 8 nm × 8 nm was used. The number of macroparticles in the cell was set such that the number of particles per cell (ppc) was comparable to the number density in units of critical density (n_c) for C, H, and electrons. To minimize the computational cost, a reduced number of ppc was used for the BN layer behind the ppC:H set to 25 ppc for B and 16 ppc for N. The electron ppc in this region was also capped to 81 ppc. WarpX implements a nuclear collisional algorithm outlined in [44] to enable the calculation of fusion reactions, including the pB reaction.

3 Results

3.1 Target characterization

The concept of macroscopic kinetics of plasma polymerization considers the energy delivered per precursor molecule during its residence in the plasma [45]. At low specific energy, precursors undergo little fragmentation and integrate into the growing film, mostly preserving their chemical motif. At high specific energy, significant fragmentation occurs, and the film grows from random molecular fragments, losing the chemical identity of the precursor. Plasma-assisted evaporation of polymers obeys the same macroscopic concept, with the only difference that precursors are not low-molar-mass molecules, but larger oligomers. Vacuum thermal decomposition of poly(ethylene) releases a flux of oligoethylenes with a mean molar mass of 1,400 g/mol, which corresponds to 100 CH_2 units in the macromolecular chain [28]. An essential part of the fragmentation of hydrocarbons in plasma is the cleavage of C-H bonds with loss of atomic hydrogen, which leads to a deficit of hydrogen in the resultant coating. Since hydrogen is one of the only two reactants in pB fusion, special care should be taken to maximize its retention in plasma polymers.

TABLE 2 Elemental content of oligoethylene thin films (in at. %) deposited with and without plasma assistance, as detected by XPS and RBS/ERDA, and density of ppC:H films.

Sample	XPS		RBS/ERDA				Film density [kg/m^3]/Thickness ellipsometry [nm]
	C	O	C	H	O	H/C	
no plasma	99.7	0.3	34.0 ± 0.7	66.0 ± 3.3	0.0 ± 0.0	1.94	620 ± 390/445
15 W	98.0	2.0	34.0 ± 0.7	64.0 ± 3.2	2.0 ± 0.04	1.88	890 ± 410/780
50 W	97.1	2.9	35.5 ± 0.7	62.0 ± 3.1	2.5 ± 0.05	1.76	1650 ± 285/2000

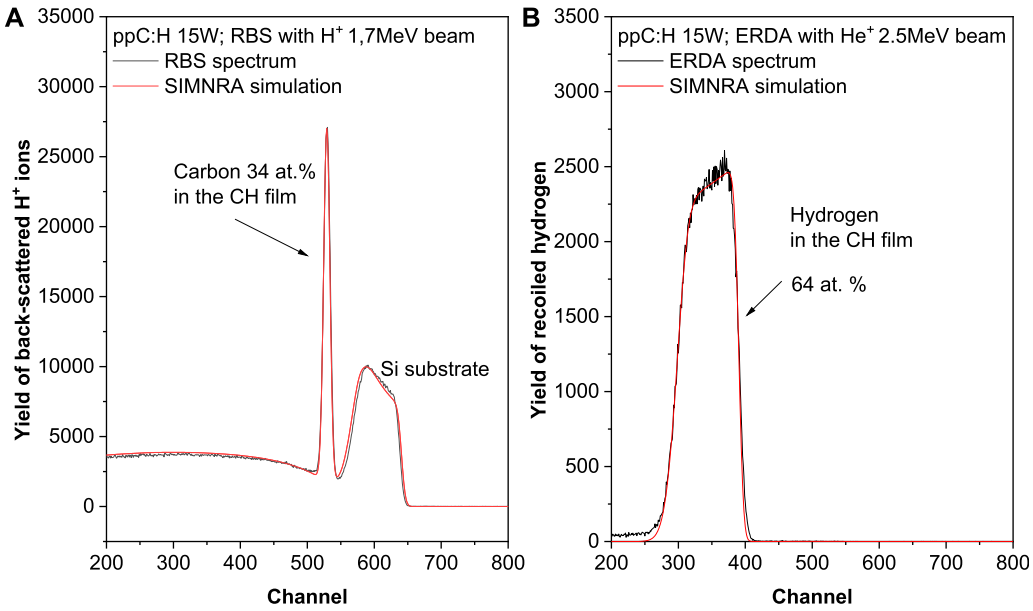

FIGURE 2
(A) RBS spectrum of pp:CH 15 W using H^+ ion beam of 1.7 MeV energy shows enhanced carbon signal in the deposited layer and **(B)** complementary measurement by He^+ ions in ERDA shows H homogeneous distribution within the layer. The thickness was indicated as 4,900×10^{15} atoms/cm^2.

Three types of ppC:H samples were prepared with 15 and 50 W plasma and without plasma, and their elemental content was analyzed by XPS and RBS/ERDA (Table 2). Although XPS is a surface-sensitive technique (the analysis depth is up to 10 nm) and RBS/ERDA probes the bulk of the film (the analysis depth is micrometers), both methods provide remarkably similar results, confirming that only hydrocarbons are present in the films. Simultaneously, XPS is not capable of detecting H, which is done by ERDA. No contamination from other elements is detected except for oxygen, which becomes incorporated into the films deposited with the plasma assistance because of post-deposition oxidation. The aging of plasma polymers is well documented; it is attributed to reactions of atmospheric oxygen with unquenched carbon radicals present in such films, with the higher plasma power leading to more drastic oxidation [46–48]. It is worth noting that in our case the concentration of oxygen does not exceed 3 at%, even for the highest power of 50 W used, which means that the depositions are performed in a power-deficient regime, with good retention of the chemical pattern of the precursor. Indeed, the RBS/ERDA data indicate that the H/C ratio is close to that of PE (H/C = 2.0) for all types of films. The H/C ratio decreases with plasma power, pointing to a cleavage of C-H bonds that occurs in oligomers due to electron impact in the gas phase and in the growing film due to ion bombardment, and hence to a partial loss of hydrogen. As an illustrative example, we present an RBS spectrum of the 15 W ppC:H sample showing high signal of C in non-Rutherford scattering which is measured using H^+ ions at 1.7 MeV resonant energy in Figure 2A. We see homogeneous C distribution accompanied with H distribution measured by ERDA in Figure 2.b. However, its absolute concentration is still more than 60 at%, even in the 50 W film, which also supports the idea that these films belong to a class of soft plasma polymers as opposed to hard hydrogenated carbon coatings [49]. The ppC:H can be customized and adapted on the specific laser-driven pB experiments by simply changing the power delivered to the plasma.

In more detail, the chemical composition of the ppC:H films was analyzed by high-resolution XPS, NMR, and FTIR spectroscopy. The C 1s XPS spectra (Figure 3A) are symmetric and perfectly overlap for all three films, confirming that the plasma assistance followed by the subtle oxidation does not influence the aliphatic

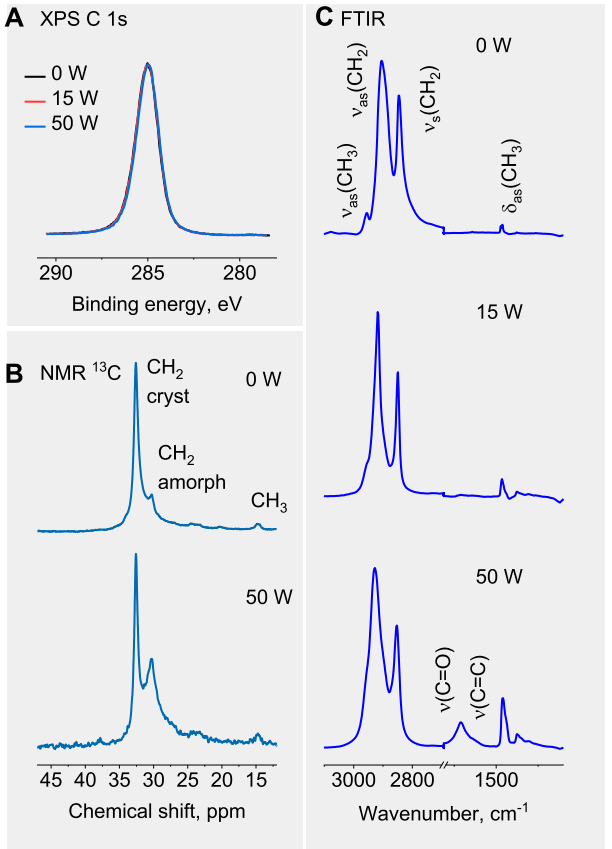

FIGURE 3
Chemical composition of ppC:H films deposited with and without plasma: **(A)** overlayed XPS C 1s spectra; **(B)** ^{13}C CP/MAS NMR spectra (adapted from [50] with permission from Wiley-VCH); **(C)** FTIR-RAS spectra.

character of the plasma polymers. Our previous NMR studies (Figure 3B) showed that the ^{13}C CP/MAS spectra are dominated by the CH_2 groups with a sharp resonance at 32.6 ppm accompanied by a weaker shoulder at 30.3 ppm [50]. The dominant peak and the shoulder belong to the crystalline and amorphous phases of oligoethylenes [51]. The NMR detection of the crystalline order is also in line with our earlier XRD studies that found a high degree of crystallinity and specified an orthorhombic structure in such films with lattice parameters matching those of poly(ethylene) [52]. The contribution from the amorphous phase is enhanced in the plasma polymerized film, which reflects the deterioration of the short- and long-range order. Nevertheless, the amorphization is not complete in contrast to an entirely amorphous character of typical plasma polymers.

The NMR spectra are also characterized by the presence of a minor signal at 14.6 ppm from the CH_3 groups, which serve as end- or side-groups in branched poly(ethylenes). The resolution of the NMR spectra does not allow us to distinguish whether the contribution from the CH_3 groups changes with plasma power; however, complementary FTIR measurements provide such information (Figure 3C). Expectedly, the dominant FTIR peaks at 2,905 cm^{-1} and 2,847 cm^{-1} belong to the asymmetric and symmetric stretching vibrations of the CH_2 groups, whereas weaker stretching and deformation vibrations of the CH_3 groups are manifested at 2,957 cm^{-1} and 1464 cm^{-1} [53]. With increasing plasma power, both types of vibrations are enhanced, with stretching vibrations submerging into those of the CH_2 groups. Furthermore, a broad band develops in the midspectral range, which is contributed by the stretching vibrations of the C=O (1,715 cm^{-1}) and C=C (1,655 cm^{-1}) functionalities. The appearance of these unprotonated moieties agrees with the observed oxidation and deprotonation of the ppC:H films, while the enhancement of the CH_3 groups points to an enhanced macromolecular branching and to a decrease in order.

Interestingly, subtle changes in the chemical landscape of the ppC:H films contrast with a substantial deviation in the film density (Table 2). The film deposited without plasma shows a density of 620 kg/m^3, which is significantly lower than ~900 kg/m^3 of conventional poly(ethylene). Vapor-deposited oligoethylenes are known to undergo self-organization phenomena at a solid interface, forming multi-terrace islands with a large portion of unoccupied space in between [52]. Although the porosity of thick coatings has not been studied, it can be hypothesized that they also contain a significant number of voids that decrease the net density of the material. The use of plasma during deposition brings a competing contribution of the active species from the gas phase. Radicals participating in the recombination reactions and ions bombarding the growing film intervene with the island growth by inducing cross-linking and densification of the film. Thus, the films prepared with plasma of 15 W and, to a larger extent, with plasma of 50 W are characterized by a higher cross-link density, shorter molecular chains between junctions, and a higher net density of the coatings, which reaches 1650 kg/m^3 for the 50 W ppC:H.

For the preparation of targets for pB fusion, the same ppC:H films were deposited using BN as substrates, and their morphology was investigated. Figure 4A shows the AFM height images and compares the 15 W ppC:H 800 nm-thick film deposited on BN and on polished Si. The surface of the ppC:H/BN sample is very rough, with the surface profile fluctuating on a micrometer scale, as can be seen from the *z*-axis of the image. The same film deposited on Si is much smoother and its surface profile fluctuates in the tens of nanometers scale. Thus, the intrinsic morphology of the ppC:H film should not significantly affect the overall morphology of the targets, which is predominantly given by the surface morphology of BN substrates.

This finding is further supported by the dependence of the RMS roughness of the ppC:H/BN samples measured for different AFM scan sizes (Figure 4B). No significant difference is found between the films deposited at different powers, evidencing that the roughness is given by BN. For the sake of argument, it can be observed that the dependence is linear in log-log coordinates, giving a notable value of the roughness exponent α = 1.0, which points to a self-affine character of the BN surface [54].

The structure of the ppC:H/BN samples was also studied by SEM/EDX. A cross-sectional SEM image of the 15 W ppC:H sample reveals a highly porous structure of BN, which is a result of the hot-press sintering of BN powder used for its production (Figure 4C, other samples are not shown as they provide similar results). The high roughness of the surface does not allow us to distinguish the ppC:H layer and investigate its possible penetration into the pores. However, the EDX analysis helps to solve this issue. Figure 4D shows the EDX images of a cross-sectional area coded in different colors for

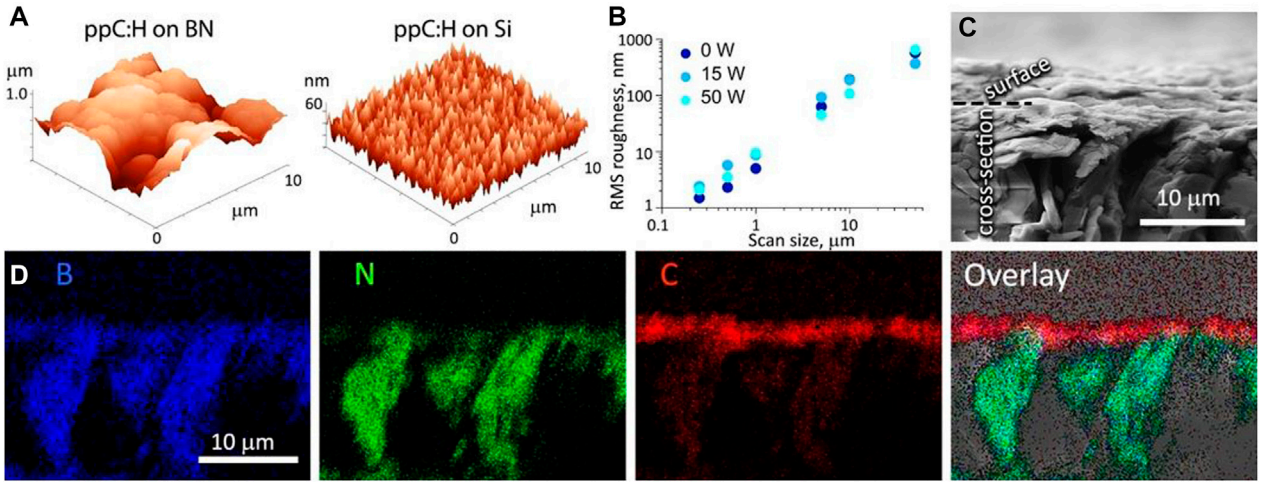

FIGURE 4
Topography and structure of ppC:H films: **(A)** AFM height images of 15 W ppC:H film deposited on BN and on Si; **(B)** AFM RMS roughness vs scan size; **(C)** cross-sectional SEM image of 15 W ppC:H film deposited on BN; **(D)** cross-sectional elemental map distribution measured by EDX on the same sample.

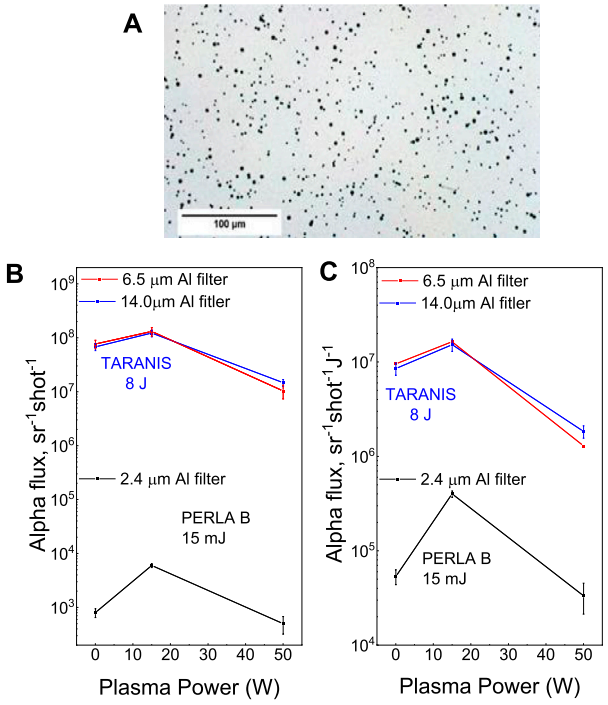

FIGURE 5
(A) Optical microscope image of a CR-39 detector after irradiation with the TARANIS laser and etching in 6.25 M of NaOH at 70°C for 1 h; **(B)** alpha particles flux generated from pB fusion using TARANIS and PERLA B lasers with different Al filters on three ppC:H/BN targets; **(C)** comparison of pB fusion efficiency using the TARANIS and PERLA B lasers (normalized to the energy delivered on the target).

individual elements of boron, nitrogen, and carbon, and the overlay of all the colors. The black voids in the images correspond to the out-of-focus areas. Boron and nitrogen are found to overlap homogeneously in the same regions, confirming that the material is boron nitride. The carbon signal is strongly enhanced in the surface area, and its thickness corresponds to a 1 µm thickness of the ppC:H film. No noticeable penetration of the plasma polymer into deeper regions can be seen, which confirms that ppC:H grows on the surface, replicating the morphology of the underlying BN substrate.

3.2 Laser-driven pB fusion: Experiments and simulations

As pointed out in Section 2.3, three types of ppC:H/BN samples were used in the experiment at TARANIS and PERLA B lasers. Figure 5A shows an example of optical microscope image taken on the CR-39 detector, which was irradiated by charged particles generated during the interaction of the 15 W ppC:H target with the TARANIS laser. After the irradiation, the CR-39 were etched in a solution of NaOH at 70°C as described in [55, 56]. The exposed tracks match the size of the tracks in the calibration of the alpha particles pointing to an efficient generation of pB fusion events triggered by the TARANIS laser. The same effect was achieved using the PERLA B laser for which the results have already been presented in [33].

The alpha particles flux recorded during the TARANIS campaign was 7×10^7, 1×10^8 and 1×10^7 α/sr/shot using 0, 15 and 50 W ppC:H, respectively. However, during the PERLA B campaign values of 8×10^2, 6×10^3 and 5×10^2 α/sr/shot were measured using the same types of targets. Expectedly, the alpha particles flux was found to be many orders of magnitude lower for the 15-mJ PERLA B laser as compared to the 8-J TARANIS laser (Figure 5B). However, the difference becomes less drastic if the alpha particles flux is normalized by the laser energy (Figure 5C). For example, the 15 W ppC:H/BN sample gives 40 times difference in pB fusion efficiency between the two laser systems. This difference can be tentatively explained by considering the cross section of the pB fusion. Indeed, the PERLA B laser triggers pB fusion through the

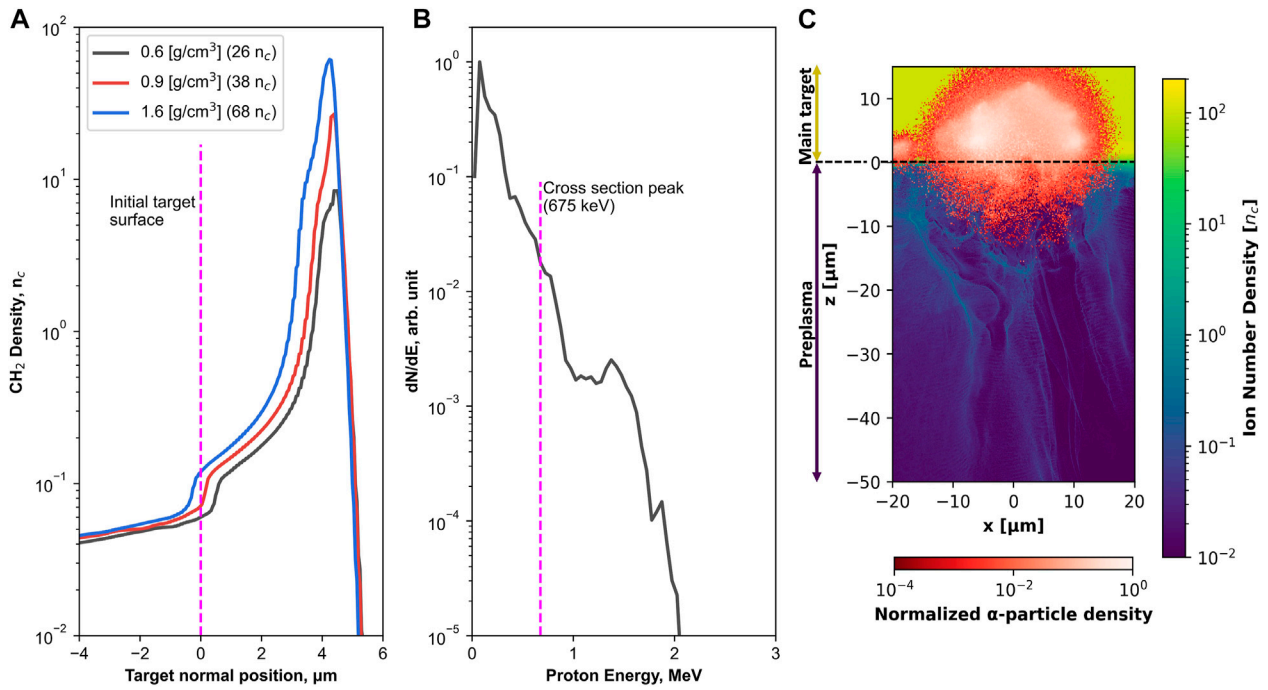

FIGURE 6
(A) Results of a FLASH simulation showing the effect of a 1.5 ns pedestal of the TARANIS laser on 1 μm ppC:H with different densities deposited on a 5 μm BN target. The initial density of the ppC:H deposition is provided in the figure legend. **(B)** Proton energy distribution, within the BN region, 1.7 ps following the interaction of the main pulse using 15 W ppC:H-BN target. **(C)** A colourmap of the normalized alphas particle densities plotted over the ion density, showing alpha particles generation occurring within the target, 600 fs after the peak intensity of the laser pulse.

first resonant peak of 165 keV [57] with a moderate number of protons (the proton cutoff energy is only slightly above this value), whereas the TARANIS laser produces a high proton flux around the main resonant peak at 670 keV (proton cutoff energies are well above this value). Considerations about the efficiency of the experiments with the two different lasers will be discussed in the simulation section. The normalized alpha particles flux for 15 W is 10^7 α/sr/J, i.e., in line with the energy conversion values obtained in the recent years as summarized in [22].

A somewhat surprising relationship can be found considering the dependence of the alpha particle yield on the properties of the ppC:H thin films. While the expected result would be a monotonous dependence on the plasma power, our study shows that the 15 W ppC:H sample is superior to the other two samples, and the trend is strikingly similar for both laser systems used. Our characterization of the targets reveals that the morphology and roughness of the surface are governed by the structure of BN, which is similar for all three samples. The hydrogen content decreases with power, but gradually and to a small extent, so it can hardly explain the observed kink in the 15 W ppC:H sample. The film density was found to be the only parameter that changes drastically with power, although its dependence is also monotonous.

3.3 Simulations results

Using the FLASH code, the interaction between the 1.5 ns pedestal, with a ns contrast of 10^{-7}, of the TARANIS laser with the target surface was modelled. The target was composed of a 1 μm ppC:H film, on top of a 5 μm BN layer. Note that both the BN substrate and ppC:H are modeled as homogeneous slabs without any voids within the simulation region. This is rationalized by the surface roughness measurements presented in Figures 4A, B showing that the variation of deposition thickness is on the order of tens of nm, which will be quickly homogenized by the pedestal. The same batch of BN was used for all depositions, therefore, the surface variation is considerable the same for all targets. A simulation was performed for each ppC:H density (600 kg/m^3, 900 kg/m^3 and 1,650 kg/m^3). The density of CH_2 along the target normal for each ppC:H deposition is shown in Figure 6A. The density profiles show that there has been some ablation and compression of the target surface by the pedestal. However, for all three deposition densities, despite the relatively low ns contrast of the TARANIS laser, following a 1.5 ns pedestal, there remains a dense region of CH_2 on the target surface with which the main pulse will interact. There appears to be minimal variation between the simulations for the three different targets in the underdense preplasma extending beyond 5 μm in front of the target surface. The output of the FLASH simulations was used as initial conditions for particle-in-cell simulations to model the interaction with the main laser pulse using the WarpX PIC code. The boron and nitrogen ions were given an initial ionization level of 3^+ and 5^+, respectively. The hydrogen and carbon ions were fully ionized during the hydrodynamic simulation.

Figure 6B shows the energy distribution of protons that are within the high boron density region (i.e., > 1 μm into the target)

1.7 ps after the main pulse. The proton distribution has a cutoff of above 2 MeV. Therefore, using the TARANIS laser, it is possible to accelerate protons into the BN target with energies in excess of the main cross-section resonance (1.4 b [57] at 670 keV in order to drive fusion reactions in this regime. The pair-wise fusion model was enabled in the WarpX simulation, allowing the generation of alpha particles through the pB fusion reaction to occur within the PIC simulation. Figure 6C displays the normalized density distribution of alpha particles plotted over the number density of the other ions, 600 fs after the peak laser intensity. This plot shows that most of the alpha particle generation occurs within the first 10 μm of the target surface, driven primarily by protons accelerated forward into the BN target. Considering the proximity of alpha particle generation to the target surface and the reduction of electronic stopping in an ionized plasma, which is discussed in [23], many of the alpha particles generated within the BN target will escape the target and reach the CR-39 detectors. It has not yet been possible to understand the trend in alpha particle yield, the deposition density and morphology that is observed experimentally.

In comparison, the simulations performed in [33], modelling the interaction between the PERLA B laser and the 680 nm ppC:H deposition on a BN target suggest that the energy cutoff of the protons accelerated forward is only 30 keV, whereas the backward accelerate proton cutoff extends to 300 keV. Therefore, it is suggested that when using the PERLA B laser, pB fusion occurs in the preplasma driven by protons accelerated to energies above the lower, secondary resonance peak of 0.1 b at 165 keV. The simulations performed to model the interaction of the TARANIS and PERLA B lasers and ppC:H-BN targets show a clear variation in the acceleration mechanism responsible for driving the pB fusion reactions. For future implementations of ppC:H-BN targets it will be important to consider the density, morphology, and thickness of the deposition to optimize the acceleration processes and the resulting fusion yield.

As discussed in the experimental results, the alpha particle yield normalized by laser energy is reduced when the PERLA B laser is used compared to the TARANIS laser. Considering the PIC simulations, the TARANIS laser can accelerate protons to energies above the main cross section resonance (670 keV), where the cross section is both over an order of magnitude higher, and covers a significantly broader energy range, than the secondary cross-section resonance. Secondly, in the PERLA B setup [33], the density of boron ions in the preplasma, obtained in simulations, was only 5×10^{19} cm^{-3} [33]. However, the simulations performed to benchmark the TARANIS experimental results show that fusion occurs in the solid BN target, where the boron ion density is much higher at 5×10^{22} cm^{-3}. This difference also affects the alpha particle yield, which depends not only on the density of the boron ions but also on the effective proton range through the target.

4 Conclusion

The films were prepared using plasma-assisted vapour phase deposition by evaporating poly(ethylene) at different discharge powers or without using plasma. Under the chosen conditions, soft plasma polymer films were prepared with a chemical structure strongly resembling that of the precursor. The plasma polymerized films are found to be prone to slight post-deposition oxidation due to reactions of unquenched radicals with ambient oxygen. Importantly, the films are rich in hydrogen: the hydrogen content reaches 66 at% in the film deposited without plasma and it slightly decreases to 62 at% as a result of the electron impact cleavage of the C-H bonds when the plasma is applied. We successfully triggered the pB fusion using 1 μm hydrocarbon plasma polymer films deposited on BN and subjected to irradiation using two different lasers: the TW-class TARANIS and the GW-class PERLA B. Regardless of the decrease in the hydrogen content, these films prove to be good candidates for triggering the pB fusion. The alpha particles yield reached 10^5/sr/J using PERLA B and 10^7/sr/J using TARANIS. An unexpected phenomenon was registered in terms of the dependence of the alpha particles yield on the properties of the plasma polymers: a maximum alpha particles generation was detected for the film deposited at medium plasma power, while the films prepared without plasma or with higher plasma power produced a lower alpha particles yield. The influence of the sample roughness and hydrogen content was excluded because the films replicate the micrometer-scale morphology of the BN substrate and retain hydrogen to a similar extent. The films have a significantly different density, which is given by denser packing of molecular segments at higher plasma powers. As shown from the simulations referring to the TARANIS campaign, protons from these deposition films can be effectively accelerated to the desired energies to drive pB fusion reactions but could not explain the experimentally observed variation in alpha particles yield between the three depositions. However, *ad hoc* hybrid simulations capable to implement the prepulse (Hydrodynamic), kinetics (PIC) and nuclear fusions are under investigation and will be topic of future studies. This work pointed out the need of customized targets optimized according to the laser parameters and the importance of the target characterization. Nevertheless, we have obtained encouraging results demonstrating that environmentally benign plasma-assisted technology can be applied to tailor the laser-target interaction, to optimize energy absorption and promote laser-driven pB fusion, with future direction for the synthesis of nanostructured boron/hydrocarbon materials.

Data availability statement

The original contributions presented in the study are included in the article/supplementary material, further inquiries can be directed to the corresponding authors.

Author contributions

In particular, AC, DM, LG, MB, SK, AP, and HB, contribute to the funding, organization and preparation of the experiments and travel costs. MT, DM, AaM, MP, KB, GN, PM, and CH, contribute to the experimental run in TARANIS and took care of the diagnostics. MT, and TF performed the CR-39 analysis. MT, PP, DN and AC, took part of the targets manufacturing and characterization. MT, YL and VI took part in the experimental run at HiLASE. AM and RM performed the RBS/ERDA

measurements. KJ, and ZK were contributing in the FTIR and ellipsometer measurements. DM performed the radiative-hydrodynamic and PIC simulations. All authors contributed to the article and approved the submitted version.

Funding

This research was funded by the project "Target Engineering for Proton-Boron Nuclear Fusion Studies" sponsored by the UK Royal Society. This work is partially supported by the project Advanced research using high intensity laser produced photons and particles (ADONIS) CZ.02.1.01/0.0/0.0/16_019/0000789 from European Regional Development Fund (ERDF). This project has received funding from the European Union's Horizon 2020 research and innovation programme under grant agreement No 871161. YL acknowledges the support of The European Regional Development Fund and the state budget of the Czech Republic (project BIATRI: No. CZ.02.1.01/0.0/0.0/15_003/0000445).

Acknowledgments

MT thanks the support of Charles University through the student GAUK: 110-10/252390 2023 and Marvel Fusion GmbH, KB and MP also acknowledge Charles University with the student grant SVV 260 579-2023. DM acknowledge the support of the HB11 Energy studentship (R8509CPP). DM thanks the STFC Scientific Computing Department's SCARF cluster and the kelvin2 cluster at Northern Ireland High Performance Computing (NI-HPC) facility funded by EPSRC (EP/T022175) for providing computational resources. The FLASH hydrodynamic code used in this work was developed in part by the DOE NNSA- and DOE Office of Science supported Flash Center for Computational Science at the University of Chicago and the University of Rochester. This work used the open-source particle-in-cell code WarpX https://github.com/ECP-WarpX/WarpX, primarily funded by the US DOE Exascale Computing Project. Primary WarpX contributors are with LBNL, LLNL, CEA-LIDYL, SLAC, DESY, CERN, and Modern Electron. We acknowledge all WarpX contributors. Some parts of the Research (RBS, ERDA analyses) were realised at the CANAM (Center of Accelerators and Nuclear Analytical Methods LM 2011019) infrastructure and the work was supported by the MEYS under the project CANAM OP, CZ.02.1.01/0.0/0.0/16_013/0001812. We acknowledge the EUROfusion Consortium, which was funded by the European Union via the Euratom Research and Training Program (Grant agreement no. 101052200—EUROfusion).

Conflict of interest

Author MT's PhD is sponsored by Marvel Fusion GmbH in ELI-Beamlines. Author DM's PhD is sponsored by HB11 Energy Holdings Pty.

The remaining authors declare that the research was conducted in the absence of any commercial or financial relationships that could be construed as a potential conflict of interest.

Publisher's note

References

1. ITER DEMO. Available at: https://www.iter.org/proj/inafewlines (Accessed May 14, 2023).

2. Zylstra AB, Hurricane OA, Callahan DA, Kritcher AL, Ralph JE, Robey HF, et al. Burning plasma achieved in inertial fusion. *Nature* (2022) 601(7894):542–8. doi:10.1038/s41586-021-04281-w

3. Oliphant MLE, Fellow R. Experiments on the transmutation of elements hy. *Proc R Soc London, Ser A* (1933) 141:259.

4. Ruhl H, Korn G. A laser-driven mixed fuel nuclear fusion micro-reactor concept (2022). Available: http://arxiv.org/abs/2202.03170 (Accessed February 7, 2022).

5. Eliezer S, Hora H, Korn G, Nissim N, Martinez Val JM. Avalanche proton-boron fusion based on elastic nuclear collisions. *Phys Plasmas* (2016) 23(5):050704. doi:10.1063/1.4950824

6. Hora H, Eliezer S, Kirchhoff G, Nissim N, Wang J, Lalousis P, et al. Road map to clean energy using laser beam ignition of boron-hydrogen fusion. *Laser Part Beams* (2017) 35(4):730–40. doi:10.1017/S0263034617000799

7. Rostoker N, Qerushi A, Binderbauer M. Colliding beam fusion reactors. *J Fusion Energ* (2003) 22(2):83–92. doi:10.1023/B:JOFE.0000036407.10861.bc

8. Moreau DC. Potentiality of the proton-boron fuel for controlled thermonuclear fusion. *Nucl Fusion* (1977) 17:13. doi:10.1088/0029-5515/17/1/002

9. Giuffrida L, Margarone D, Cirrone GAP, Picciotto A, Cuttone G, Korn G. Prompt gamma ray diagnostics and enhanced hadron-therapy using neutron-free nuclear reactions. *AIP Adv* (2016) 6(10). doi:10.1063/1.4965254

10. Cirrone GAP, Manti L, Margarone D, Petringa G, Giuffrida L, Minopoli A, et al. First experimental proof of Proton Boron Capture Therapy (PBCT) to enhance protontherapy effectiveness. *Sci Rep* (2018) 8(1):1141. doi:10.1038/s41598-018-19258-5

11. Bláha P, Feoli C, Agosteo S, Calvaruso M, Cammarata FP, Catalano R, et al. The proton-boron reaction increases the radiobiological effectiveness of clinical low- and high-energy proton beams: Novel experimental evidence and perspectives. *Front Oncol* (2021) 11:682647. doi:10.3389/fonc.2021.682647

12. Ohlandt C. *A design study of a p-11B gasdynamic mirror fusion propulsion system*. College Park, MA.: AIP Publishing (2003). p. 490–6.

13. Pappalardo L, Romano FP, Garraffo S, De Sanoit J, Marchetta C, Pappalardo G. The improved lns pixe-alpha portable system: Archaeometric applications*. *Archaeometry* (2003) 45(2):333–9. doi:10.1111/1475-4754.00111

14. Qaim SM, Spahn I, Scholten B, Neumaier B. Uses of alpha particles, especially in nuclear reaction studies and medical radionuclide production. *Radiochim Acta* (2016) 104(9):601–24. doi:10.1515/ract-2015-2566

15. Szkliniarz K, Sitarz M, Walczak R, Jastrzębski J, Bilewicz A, Choiński J, et al. Production of medical Sc radioisotopes with an alpha particle beam. *Appl Radiat Isot* (2016) 118:182–9. doi:10.1016/j.apradiso.2016.07.001

16. Margarone D, Krasa J, Picciotto A, Torrisi L, Laska L, Velyhan A, et al. High current, high energy proton beams accelerated by a sub-nanosecond laser. *Nucl Instr Methods Phys Res Section A: Acc Spectrometers, Detectors Associated Equipment* (2011) 653:159–63. doi:10.1016/j.nima.2010.12.118

17. Clark EL, Krushelnick K, Davies JR, Zepf M, Tatarakis M, Beg FN, et al. Measurements of energetic proton transport through magnetized plasma from intense laser interactions with solids. *Phys Rev Lett* (2000) 84(4):670–3. doi:10.1103/PhysRevLett.84.670

18. Belyaev VS, Matafonov AP, Vinogradov VI, Krainov VP, Lisitsa VS, Roussetski AS, et al. Observation of neutronless fusion reactions in picosecond laser plasmas. *Phys Rev E Stat Nonlin Soft Matter Phys* (2005) 72(2):026406. doi:10.1103/PhysRevE.72.026406

19. Labaune C, Baccou C, Depierreux S, Goyon C, Loisel G, Yahia V, et al. Fusion reactions initiated by laser-accelerated particle beams in a laser-produced plasma. *Nat Commun* (2013) 4:2506. doi:10.1038/ncomms3506

20. Picciotto A, Margarone D, Velyhan A, Bellutti P, Krasa J, Szydlowsky A, et al. Boron-proton nuclear-fusion enhancement induced in boron-doped silicon targets by low-contrast Pulsed Laser. *Phys Rev X* (2014) 4(3):031030. doi:10.1103/PhysRevX.4.031030

21. Margarone D, Picciotto A, Velyhan A, Krasa J, Kucharik M, Mangione A, et al. Advanced scheme for high-yield laser driven nuclear reactions. *Plasma Phys Control Fusion* (2015) 57(1):014030. doi:10.1088/0741-3335/57/1/014030

22. Margarone D, Bonvalet J, Giuffrida L, Morace A, Kantarelou V, Tosca M, et al. In-target proton–boron nuclear fusion using a PW-class laser. *Appl Sci (Switzerland)* (2022) 12(3):1444. doi:10.3390/app12031444

23. Bonvalet J, Nicolaï P, Raffestin D, D'humieres E, Batani D, Tikhonchuk V, et al. Energetic α -particle sources produced through proton-boron reactions by high-energy high-intensity laser beams. *Phys Rev E* (2021) 103(5):053202. doi:10.1103/PhysRevE.103.053202

24. Schollmeier MS, Shirvanyan V, Capper C, Steinke S, Higginson A, Hollinger R, et al. Investigation of proton beam-driven fusion reactions generated by an ultra-short petawatt-scale laser pulse. *Laser Part Beams* (2022) 2022:1–13. doi:10.1155/2022/2404263

25. Giuffrida L, Belloni F, Margarone D, Petringa G, Milluzzo G, Scuderi V, et al. High-current stream of energetic α particles from laser-driven proton-boron fusion. *Phys Rev E* (2020) 101(1):013204. doi:10.1103/PhysRevE.101.013204

26. Li S, Lu X, Lou Y, Liu K, Zou B. The synthesis and characterization of h-BN nanosheets with high yield and crystallinity. *ACS Omega* (2021) 6(42):27814–22. doi:10.1021/acsomega.1c03406

27. Liu M, Ai X, Liu Y, Chen Q, Zhang S, He Z, et al. Fabrication of solid CH-CD multilayer microspheres for inertial confinement fusion. *Matter Radiat Extremes* (2021) 6(2). doi:10.1063/5.0033103

28. Choukourov A, Melnichuk I, Gordeev I, Kylián O, Hanuš J, Kousal J, et al. Dynamic scaling and kinetic roughening of poly(ethylene) islands grown by vapor phase deposition. *Thin Solid Films* (2014) 565:249–60. doi:10.1016/j.tsf.2014.06.029

29. Bonvalet J. Energetic α-particle sources produced by high energy, high intensity laser beams. *Phys Rev E* (2021) 103:053202. doi:10.1103/PhysRevE.103.053202

30. Choukourov A, Pleskunov P, Nikitin D, Tafiichuk R, Shelemin A, Hanuš J, et al. Plasma-assisted growth of polyethylene fractal nano-islands on polyethylene oxide films: Impact of film confinement and glassy dynamics on fractal morphologies. *Appl Surf Sci* (2019) 489:55–65. doi:10.1016/j.apsusc.2019.05.287

31. Choukourov A, Gordeev I, Ponti J, Uboldi C, Melnichuk I, Vaidulych M, et al. Microphase-separated PE/PEO thin films prepared by plasma-assisted vapor phase deposition. *ACS Appl Mater Inter* (2016) 8(12):8201–12. doi:10.1021/acsami.5b12382

32. Yasuda H. Glow discharge polymerization. *Glow discharge polymerization* (1981) 16:199–293. doi:10.1002/pol.1981.230160104

33. Istokskaia V, Tosca M, Giuffrida L, Psikal J, Grepl F, Kantarelou V, et al. A multi-MeV alpha particle source via proton-boron fusion driven by a 10-GW tabletop laser. *Commun Phys* (2023) 6(1):27. doi:10.1038/s42005-023-01135-x

34. Drabik M, Kousal J, Pihosh Y, Choukourov A, Biederman H, Slavinska D, et al. Composite SiOx/hydrocarbon plasma polymer films prepared by RF magnetron sputtering of SiO2 and polyimide. *Vacuum* (2007) 81(7):920–7. doi:10.1016/j.vacuum.2006.10.013

35. Choukourov A, Pihosh Y, Stelmashuk V, Biederman H, Slavinská D, Kormunda M, et al. Rf sputtering of composite SiO/plasma polymer films and their basic properties. *Surf Coat Tech* (2002) 151-152:214–7. doi:10.1016/S0257-8972(01)01622-X

36. Dzelzainis T, Nersisyan G, Riley D, Romagnani L, Ahmed H, Bigongiari A, et al. The TARANIS laser: A multi-terawatt system for laser-plasma investigations. *Laser Part Beams* (2010) 28(3):451–61. doi:10.1017/S0263034610000467

37. Smrž M, Novák O, Mužík J, Turčičová H, Chyla M, Nagisetty S, et al. Advances in high-power, ultrashort pulse DPSSL technologies at HiLASE. *Appl Sci* (2017) 7(10):1016. doi:10.3390/app7101016

38. Mayer M. SIMNRA, a simulation program for the analysis of NRA, RBS and ERDA. In: AIP Conference Proceedings; Lausanne, Switzerland (1999). p. 541–4. doi:10.1063/1.59188

39. Roussetski AS. Application of CR-39 plastic track detector for detection of DD and DT-reaction products in cold fusion experiments. In: 8th International Conference on Cold Fusion; May, 21-26 2000; Bologna, Italy. Italian Physical Society (2000).

40. Kuchera MP, Tarasov OB, Bazin D, Sherril B, Tarasova KV. LISE++ software updates and future plans. *J Phys Conf Ser* (2015) 664:072029. doi:10.1088/1742-6596/664/7/072029

41. Kantarelou V, Velyhan A, Tchórz P, Rosiński M, Petringa G, Cirrone GAP, et al. A methodology for the discrimination of alpha particles from other ions in laser-driven proton-boron reactions using CR-39 detectors coupled in a thomson parabola spectrometer. *Laser Part Beams* (2023) 2023:1–12. doi:10.1155/2023/3125787

42. Fryxell B, Olson K, Ricker P, Timmes FX, Zingale M, Lamb DQ, et al. Flash: An adaptive mesh hydrodynamics code for modeling astrophysical thermonuclear flashes. *Astrophys J Suppl Ser* (2000) 131(1):273–334. doi:10.1086/317361

43. Fedeli L, Huebl A, Boillod-Cerneux F, Clark T, Gott K, Hillairet C, et al. Pushing the frontier in the design of laser-based electron accelerators with groundbreaking mesh-refined particle-in-cell simulations on exascale-class supercomputers. In: SC22: International Conference for High Performance Computing, Networking, Storage and Analysis; November 13-18, 2022; Dallas, TX. IEEE (2022). p. 1–12. doi:10.1109/SC41404.2022.00008

44. Higginson DP, Link A, Schmidt A. A pairwise nuclear fusion algorithm for weighted particle-in-cell plasma simulations. *J Comput Phys* (2019) 388:439–53. doi:10.1016/j.jcp.2019.03.020

45. Hegemann D, Hossain MM, Körner E, Balazs DJ. Macroscopic description of plasma polymerization. *Plasma Process Polym* (2007) 4(3):229–38. doi:10.1002/ppap.200600169

46. Kholodkov I, Biederman H, Slavínská D, Choukourov A, Trchova M. Plasma polymers prepared by RF sputtering of polyethylene. *Vacuum* (2003) 70(4):505–9. doi:10.1016/S0042-207X(02)00702-9

47. Whittle JD, Short RD, Douglas CWI, Davies J. Differences in the aging of allyl alcohol, acrylic acid, allylamine, and octa-1,7-diene plasma polymers as studied by X-ray photoelectron spectroscopy. *Chem Mater* (2000) 12(9):2664–71. doi:10.1021/cm0002158

48. Gengenbach TR, Vasic ZR, Chatelier RC, Griesser HJ. A multi-technique study of the spontaneous oxidation of N-hexane plasma polymers. *J Polym Sci A Polym Chem* (1994) 32(8):1399–414. doi:10.1002/pola.1994.080320801

49. Robertson J. Diamond-like amorphous carbon. *Mater Sci Eng R: Rep* (2002) 37(4-6):129–281. doi:10.1016/S0927-796X(02)00005-0

50. Hanuš J, Hanyková L, Choukourov A, Kousal J, Polonskyi O, Slavínská D, et al. NMR study of polyethylene-like plasma polymer films. *Plasma Process Polym* (2009) 6(1):S362–5. doi:10.1002/ppap.200930802

51. Hu W-G, Schmidt-Rohr K. Characterization of ultradrawn polyethylene fibers by NMR: Crystallinity, domain sizes and a highly mobile second amorphous phase. *Polymer (Guildf)* (2000) 41(8):2979–87. doi:10.1016/S0032-3861(99)00429-2

52. Choukourov A, Melnichuk I, Gordeev I, Nikitin D, Tafiichuk R, Pleskunov P, et al. Self-organization of vapor-deposited polyolefins at the solid/vacuum interface. *Prog Org Coat* (2020) 143:105630. doi:10.1016/j.porgcoat.2020.105630

53. Richard N. *Interpreting infrared, Raman, and nuclear magnetic resonance spectra*. Cambridge, MA: Academic Press (2001).

54. Pelliccione M, Lu T-M. *Evolution of thin film morphology*. New York, NY: Springer (2008). doi:10.1007/978-0-387-75109-2

55. Guo SL, Chen BL, Durrani SA. Solid-state nuclear track detectors. In: *Handbook of radioactivity analysis*. Amsterdam, Netherlands: Elsevier Inc. (2012). p. 233–98.

56. Tonelli AE, Gomez MA, Tanaka H, Cozine MH. Chapter 4 solid state 13C NMR studies of the structures, conformations, and dynamics of semi· crystalline polymers. In: *Solid state NMR of polymers*. Boston: Springer (1991).

57. Sikora MH, Weller HR. A new evaluation of the ^{11}B(p,α)$\alpha\alpha$ reaction rate. *J Fusion Energ* (2016) 35(3):538–43. doi:10.1007/s10894-016-0069-y